Silicon photonic micro-disk resonators for label-free biosensing

Samantha M. Grist,[1,3,*] Shon A. Schmidt,[2,3] Jonas Flueckiger,[1] Valentina Donzella,[1] Wei Shi,[1] Sahba Talebi Fard,[1] James T. Kirk,[2] Daniel M. Ratner,[2] Karen C. Cheung,[1] and Lukas Chrostowski[1]

[1]*Department of Electrical and Computer Engineering, The University of British Columbia, 2332 Main Mall, Vancouver, BC. V6T 1Z4, Canada*

[2]*Department of Bioengineering, The University of Washington, 3720 15th Ave NE, Seattle, WA 98195-5061, USA*

[3]*These authors contributed equally to this work.*

[*]*sgrist@ece.ubc.ca*

Abstract: Silicon photonic biosensors are highly attractive for multiplexed Lab-on-Chip systems. Here, we characterize the sensing performance of 3 μm TE-mode and 10 μm dual TE/TM-mode silicon photonic micro-disk resonators and demonstrate their ability to detect the specific capture of biomolecules. Our experimental results show sensitivities of 26 nm/RIU and 142 nm/RIU, and quality factors of $3.3x10^4$ and $1.6x10^4$ for the TE and TM modes, respectively. Additionally, we show that the large disks contain both TE and TM modes with differing sensing characteristics. Finally, by serializing multiple disks on a single waveguide bus in a CMOS compatible process, we demonstrate a biosensor capable of multiplexed interrogation of biological samples.

OCIS codes: (280.0280) Remote sensing and sensors; (280.1415) Biological sensing and sensors.

References and Links

1. A. L. Washburn and R. C. Bailey, "Photonics-on-a-chip: recent advances in integrated waveguides as enabling detection elements for real-world, lab-on-a-chip biosensing applications," Analyst (Lond.) **136**(2), 227–236 (2010).
2. L. Chrostowski, S. Grist, J. Flueckiger, W. Shi, X. Wang, E. Ouellet, H. Yun, M. Webb, B. Nie, Z. Liang, K. Cheung, S. Schmidt, D. Ratner, and N. Jaeger, "Silicon photonic resonator sensors and devices," Proc. SPIE **8236**, 823620 1–16 (2012).
3. A. L. Washburn, L. C. Gunn, and R. C. Bailey, "Label-free quantitation of a cancer biomarker in complex media using silicon photonic microring resonators," Anal. Chem. **81**(22), 9499–9506 (2009).
4. A. L. Washburn, M. S. Luchansky, A. L. Bowman, and R. C. Bailey, "Quantitative, label-free detection of five protein biomarkers using multiplexed arrays of silicon photonic microring resonators," Anal. Chem. **82**(1), 69–72 (2010).
5. N. M. Jokerst, L. Luan, S. Palit, M. Royal, S. Dhar, M. Brooke, and T. Tyler, "Progress in chip-scale photonic sensing," IEEE Trans. Biomed. Circuits Syst. **3**(4), 202–211 (2009).
6. M. Iqbal, M. A. Gleeson, B. Spaugh, F. Tybor, W. G. Gunn, M. Hochberg, T. Baehr-Jones, R. C. Bailey, and L. C. Gunn, "Label-free biosensor arrays based on silicon ring resonators and high-speed optical scanning instrumentation," IEEE J. Sel. Top. Quantum Electron. **16**(3), 654–661 (2010).
7. K. De Vos, I. Bartolozzi, E. Schacht, P. Bienstman, and R. Baets, "Silicon-on-Insulator microring resonator for sensitive and label-free biosensing," Opt. Express **15**(12), 7610–7615 (2007).
8. C. A. Barrios, M. J. Bañuls, V. González-Pedro, K. B. Gylfason, B. Sánchez, A. Griol, A. Maquieira, H. Sohlström, M. Holgado, and R. Casquel, "Label-free optical biosensing with slot-waveguides," Opt. Lett. **33**(7), 708–710 (2008).
9. T. Claes, J. G. Molera, K. De Vos, E. Schacht, R. Baets, and P. Bienstman, "Label-free biosensing with a slot-waveguide-based ring resonator in silicon on insulator," IEEE Photonics J. **1**(3), 197–204 (2009).
10. A. M. Armani, R. P. Kulkarni, S. E. Fraser, R. C. Flagan, and K. J. Vahala, "Label-free, single-molecule detection with optical microcavities," Science **317**(5839), 783–787 (2007).
11. F. Ferrarese Lupi, D. Navarro-Urrios, J. Rubio-Garcia, J. Monserrat, C. Domínguez, and B. Garrido, "Optically active μ-disks resonators-based sensor for refractive index variation detection," Proc. SPIE **8431**, 84311B 1–8 (2012).

#184113 - $15.00 USD Received 24 Jan 2013; revised 7 Mar 2013; accepted 9 Mar 2013; published 26 Mar 2013

12. M. Soltani, S. Yegnanarayanan, and A. Adibi, "Ultra-high Q planar silicon microdisk resonators for chip-scale silicon photonics," Opt. Express **15**(8), 4694–4704 (2007).
13. S. Yegnanarayanan, W. Roman, M. Soltani, G. Cremona, H. Lu, and A. Adibi, "On-chip integration of microfluidic channels with ultra-high Q silicon microdisk resonators for lab-on-a-chip sensing applications," in *Lasers and Electro-Optics Society, 2007. LEOS 2007. The 20th Annual Meeting of the IEEE* (Institute of Electrical and Electronics Engineers, New York, 2007), pp. 50–51.
14. A. Di Falco, L. Ofaolain, and T. Krauss, "Chemical sensing in slotted photonic crystal heterostructure cavities," Appl. Phys. Lett. **94**, 063503 1–3 (2009).
15. J. Jágerská, H. Zhang, Z. Diao, N. Le Thomas, and R. Houdré, "Refractive index sensing with an air-slot photonic crystal nanocavity," Opt. Lett. **35**(15), 2523–2525 (2010).
16. P. Prabhathan, V. M. Murukeshan, Z. Jing, and P. V. Ramana, "Compact SOI nanowire refractive index sensor using phase shifted Bragg grating," Opt. Express **17**(17), 15330–15341 (2009).
17. J. T. Kirk, N. D. Brault, T. Baehr-Jones, M. Hochberg, S. Jiang, and D. M. Ratner, "Zwitterionic polymer-modified silicon microring resonators for label-free biosensing in undiluted humanplasma," Biosens. Bioelectron. **42**, 100–105 (2013).
18. I. White, H. Zhu, J. Suter, and X. Fan, "Label-free biosensing with the optofluidic ring resonator," in *Advanced Photonic Structures for Biological and Chemical Detection*, X. Fan, ed. (Springer US, 2009), pp. 377–393.
19. P. Dumon, W. Bogaerts, V. Wiaux, J. Wouters, S. Beckx, J. Van Campenhout, D. Taillaert, B. Luyssaert, P. Bienstman, D. Van Thourhout, and R. Baets, "Low-loss SOI photonic wires and ring resonators fabricated with deep UV lithography," IEEE Photon. Technol. Lett. **16**(5), 1328–1330 (2004).
20. K. K. Lee, D. R. Lim, H. C. Luan, A. Agarwal, J. Foresi, and L. C. Kimerling, "Effect of size and roughness on light transmission in a Si/SiO waveguide: experiments and model," Appl. Phys. Lett. **77**(11), 1617–1619 (2000).
21. S. Sardo, F. Giacometti, S. Doneda, U. Colombo, M. D. Muri, A. Donghi, R. Morson, G. Mutinati, A. Nottola, M. Gentili, and M. C. Ubaldi, "Line edge roughness (LER) reduction strategy for SOI waveguides fabrication," Microelectron. Eng. **85**(5-6), 1210–1213 (2008).
22. D. X. Xu, M. Vachon, A. Densmore, R. Ma, S. Janz, A. Delâge, J. Lapointe, P. Cheben, J. H. Schmid, E. Post, S. Messaoudène, and J. M. Fédéli, "Real-time cancellation of temperature induced resonance shifts in SOI wire waveguide ring resonator label-free biosensor arrays," Opt. Express **18**(22), 22867–22879 (2010).
23. W. Shi, H. Yun, W. Zhang, C. Lin, T. K. Chang, Y. Wang, N. A. F. Jaeger, and L. Chrostowski, "Ultra-compact, high-Q silicon microdisk reflectors," Opt. Express **20**(20), 21840–21846 (2012).
24. M. S. Luchansky, A. L. Washburn, T. A. Martin, M. Iqbal, L. C. Gunn, and R. C. Bailey, "Characterization of the evanescent field profile and bound mass sensitivity of a label-free silicon photonic microring resonator biosensing platform," Biosens. Bioelectron. **26**(4), 1283–1291 (2010).
25. S. A. Darst, M. Ahlers, P. H. Meller, E. W. Kubalek, R. Blankenburg, H. O. Ribi, H. Ringsdorf, and R. D. Kornberg, "Two-dimensional crystals of streptavidin on biotinylated lipid layers and their interactions with biotinylated macromolecules," Biophys. J. **59**(2), 387–396 (1991).
26. A. L. Weisenhorn, F. J. Schmitt, W. Knoll, and P. K. Hansma, "Streptavidin binding observed with an atomic force microscope," Ultramicroscopy **42-44**(Pt B), 1125–1132 (1992).
27. J. Flueckiger, S. M. Grist, G. Bisra, L. Chrostowski, and K. C. Cheung, "Cascaded silicon-on-insulator microring resonators for the detection of biomolecules in PDMS microfluidic channel," Proc. SPIE **7929**, 79290I 1–10 (2011).
28. S. Sardo, F. Giacometti, S. Doneda, U. Colombo, M. D. Muri, A. Donghi, R. Morson, G. Mutinati, A. Nottola, M. Gentili, and M. C. Ubaldi, "Line edge roughness (LER) reduction strategy for SOI waveguides fabrication," Microelectron. Eng. **85**(5-6), 1210–1213 (2008).
29. M. Gnan, D. S. Macintyre, M. Sorel, R. M. De La Rue, and S. Thoms, "Enhanced stitching for the fabrication of photonic structures by electron beam lithography," J. Vac. Sci. Technol. B **25**(6), 2034–2037 (2007).
30. Y. Chen, J. Feng, Z. Zhou, C. J. Summers, D. S. Citrin, and J. Yu, "Simple technique to fabricate microscale and nanoscale silicon waveguide devices," Front. Optoelectron. China **2**(3), 308–311 (2009).
31. Y. Chen, J. Feng, Z. Zhou, J. Yu, C. J. Summers, and D. S. Citrin, "Fabrication of silicon microring resonator with smooth sidewalls," J. Micro/Nanolithogr. MEMS MOEMS **8**, 043060 1–5 (2009).
32. S. G. Attila Mekis, G. Masini, A. Narasimha, T. Pinguet, S. Sahni, and P. D. Dobbelaere, "A grating-coupler-enabled CMOS photonics platform," IEEE J. Sel. Top. Quantum Electron. **17**, 597–608 (2011).
33. R. L. Sokoloff, K. C. Norton, C. L. Gasior, K. M. Marker, and L. S. Grauer, "A dual-monoclonal sandwich assay for prostate-specific membrane antigen: Levels in tissues, seminal fluid and urine," Prostate **43**(2), 150–157 (2000).
34. U. B. Nielsen and B. H. Geierstanger, "Multiplexed sandwich assays in microarray format," J. Immunol. Methods **290**(1-2), 107–120 (2004).
35. G. Moţa, I. Moraru, J. Sjöquist, and V. Gheţie, "Protein A as a molecular probe for the detection of antigen induced conformational change in Fc region of rabbit antibody," Mol. Immunol. **18**(5), 373–378 (1981).
36. W. L. DeLano, M. H. Ultsch, A. M. de Vos, and J. A. Wells, "Convergent solutions to binding at a protein-protein interface," Science **287**(5456), 1279–1283 (2000).
37. H. Elwing, "Protein absorption and ellipsometry in biomaterial research," Biomaterials **19**(4-5), 397–406 (1998).
38. K. P. S. Dancil, D. P. Greiner, and M. J. Sailor, "A porous silicon optical biosensor: detection of reversible binding of IgG to a protein A-modified surface," JACS **121**(34), 7925–7930 (1999).

#184113 - $15.00 USD Received 24 Jan 2013; revised 7 Mar 2013; accepted 9 Mar 2013; published 26 Mar 2013

39. M. C. Coen, R. Lehmann, P. Gröning, M. Bielmann, C. Galli, and L. Schlapbach, "Adsorption and bioactivity of protein A on silicon surfaces studied by AFM and XPS," J. Colloid Interface Sci. **233**(2), 180–189 (2001).
40. M. Graille, E. A. Stura, A. L. Corper, B. J. Sutton, M. J. Taussig, J.-B. Charbonnier, and G. J. Silverman, "Crystal structure of a Staphylococcus aureus protein A domain complexed with the Fab fragment of a human IgM antibody: structural basis for recognition of B-cell receptors and superantigen activity," Proc. Natl. Acad. Sci. U.S.A. **97**(10), 5399–5404 (2000).
41. H. P. Erickson, "Size and shape of protein molecules at the nanometer level determined by sedimentation, gel filtration, and electron microscopy," Biol. Proced. Online **11**(1), 32–51 (2009).
42. J. Vörös, "The density and refractive index of adsorbing protein layers," Biophys. J. **87**(1), 553–561 (2004).
43. I. Teraoka and S. Arnold, "Theory of resonance shifts in TE and TM whispering gallery modes by nonradial perturbations for sensing applications," J. Opt. Soc. Am. B **23**(7), 1381–1389 (2006).

1. Introduction

Silicon photonics shows promise towards revolutionizing label-free biosensing and medical diagnostics [1]. Photonic devices leveraging the silicon-on-insulator (SOI) platform can be used as sensors tuned to specific biological applications, and are readily fabricated into highly multiplexed systems for integration with microfluidics and electronics for Lab on Chip (LoC) systems. Within the biosensing field, there has been increased interest in SOI resonator-based sensors, which offer the potential to achieve high detection limits [2] while facilitating multiplexed analysis [3, 4] and reduced costs for potential point-of-care diagnostic systems [5].

Many types of SOI photonic biosensors including strip [6, 7] and slot waveguide ring resonators [8, 9], disk resonators [10–13], photonic crystals [14, 15], and Bragg gratings [2, 16], operate by sensing refractive index changes (induced by bulk solution changes or molecular binding events) in the waveguide cladding. These refractive index changes modify the modal effective index (n_{eff}), and for resonant sensors it results in a resonance wavelength (λ_{res}) shift. The change in modal effective index resulting from small changes in the refractive index in the cladding has been demonstrated [17] to be a function of the overlap integral between the electric field intensity and the changes occurring in the refractive index of the cladding over the full range of the mode cross-section. To map the changes in effective index to changes in resonance wavelength, one can use the resonance equation [6]:

$$\lambda_{res} = \frac{2\pi R n_{eff}}{m}, \tag{1}$$

where λ denotes the wavelength, m the integer mode order, and R the disk radius. As a result, the observed shift in resonance wavelength is dependent on the overlap between the electric field and the region in which the binding events or bulk changes occur. This means that modes with higher field strength outside the waveguide will yield larger wavelength shifts for the same refractive index change, and that modes with longer evanescent field penetration distances will yield resonance wavelength shifts for refractive index changes further away from the waveguide surface.

The bulk refractive index sensitivity S of a resonator is given by $S = \Delta\lambda/\Delta n_{clad}$, where Δn_{clad} is a change in cladding refractive index and $\Delta\lambda$ is the resonance wavelength shift induced by the changing cladding index. Because the resonance wavelength shift is dependent on the overlap of the electric field intensity with the cladding changes, modes with the highest amounts of the electric field traveling in the cladding (outside of the silicon waveguide) have the highest sensitivities.

Commercial surface plasmon resonance (SPR) systems are able to achieve detection limits (the minimum detectable Δn_{clad}) on the order of 10^{-7} RIU; however, this limit is a function of many parameters, including the readout instrumentation and improvements due to data processing as well as the sensor's own characteristics [18]. In order to fairly compare sensing structures without the influence of other system components, we need to define a comparison metric for resonator sensors. This minimum detectable index change for a single resonator (or

#184113 - $15.00 USD Received 24 Jan 2013; revised 7 Mar 2013; accepted 9 Mar 2013; published 26 Mar 2013

Intrinsic Limit of Detection, ILOD) may be given as the index required to shift the resonance wavelength by one linewidth and will be used throughout this paper when discussing detection limits [2]:

$$ILOD = \frac{\lambda_{res}}{QS}, \tag{2}$$

where Q is the quality factor of the resonator (the resonance wavelength divided by the peak linewidth) and S is the resonator's bulk refractive index sensitivity defined above. The quality factor of the resonator is determined by the round-trip resonator losses (composed of material, scattering, bending, substrate leakage, and mode mismatch losses [19, 20]) as well as the coupling to and from the waveguide by which the sensor is interrogated. Because the ILOD does not take readout system optimizations into account, it is usually lower than the system limit of detection; for example, the theoretical ILOD limit for a resonator in water at 1550 nm (with water absorption being the only loss mechanism) is 2.4×10^{-4} RIU [2].

Optical waveguides, depending on geometry and refractive index, can support both quasi-transverse electric (henceforth 'TE') and quasi-transverse magnetic (henceforth 'TM') optical modes. TM modes have significantly more electric field overlap with the surrounding environment in the commonly used 220 nm thick SOI waveguides [2], thus they can allow for improved sensing performance. Additionally, because the electric field primarily exists on the top and bottom waveguide surfaces, TM resonators offer the potential for reduced sidewall losses [20, 21]. TM ring resonators have previously been fabricated and demonstrated excellent sensing characteristics [22].

Disk resonators offer several potential advantages stemming from their unique structure and compact sizes. In a disk, the whispering gallery mode travels near the outside perimeter; as such, it only contacts one sidewall. This property can decrease sidewall scattering losses, thus improving Q. Additionally, disks have been reported with very small footprints (radii of 1.5-3 μm) [23]. This can make them less expensive to fabricate and can lead to lower surface mass limits of detection (as each biomolecule of a given size will have a higher overall effect on the field distribution) [24]. Furthermore, these small footprints result in a wide free-spectral range and permit future interrogation of many micro-disk sensors on a single waveguide bus, with multiple resonance peaks from multiple sensors in one FSR region of the system's optical spectrum. This feature enables high-throughput and multiplexed sensing of multiple target species using a single optical channel.

Because of these many advantages of disk resonators, in this paper we validated disk-based biosensors simultaneously using both TE and TM optical modes, and multiplexed resonators on a single waveguide bus. These devices represent valuable building blocks for LoC applications. To our knowledge, we are the first to demonstrate biosensing capabilities of disk resonators fabricated in a standard SOI process. In addition, we show results of disks supporting TE modes as well as both TE and TM modes, which could be harnessed to provide additional information about biomolecular interactions at the resonator surface. Our reported limits of detection are on the same order as the best ring-based sensors for both TE and TM devices.

2. Biosensor simulation and design

Disk resonators were simulated using an eigenmode solver (Lumerical MODE Solutions) and the finite difference time domain method (Lumerical FDTD Solutions) using previously described methods [23]. The TE and TM optical mode profiles for micro-disks were simulated in the eigensolver under varying cladding refractive indices corresponding to water and varying concentrations of table salt and their effective indices and material and bending losses exported. These wavelength-dependent effective indices, $n_{eff}(\lambda)$, were then plotted with the resonance equation (Eq. (1)) to determine the resonance wavelengths.

#184113 - $15.00 USD Received 24 Jan 2013; revised 7 Mar 2013; accepted 9 Mar 2013; published 26 Mar 2013

Comparing consecutive resonance wavelengths yields the free spectral range (FSR), while comparing the resonance wavelengths of the disk under varying cladding refractive index affords a prediction of the resonator's refractive index sensitivity. Because 3 μm and 10 μm disks are multimode, this analysis was repeated for all of the high Q whispering gallery modes present near the outer edge of the disks (two TE modes for the 3 μm, six TE and four TM modes for the 10 μm disk). Figure 1 presents the electric field intensities of the first three TE and TM modes in a 10 μm disk.

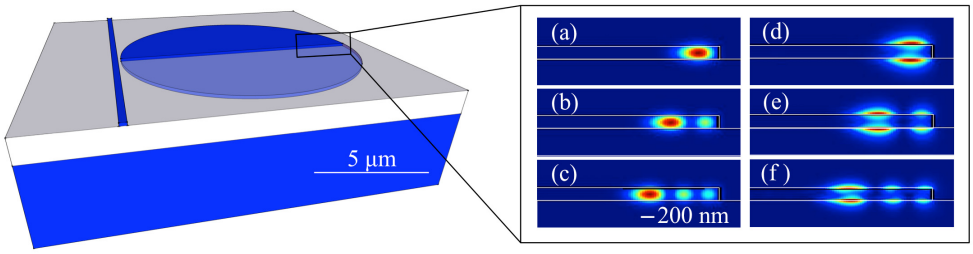

Fig. 1. Simulated mode profiles (E-intensity) for a 10 μm disk. (a)-(c) depict the first to third TE modes, while (d)-(f) depict the first to third TM modes.

It is evident from the mode profiles in Fig. 1 that the electric field of the TM modes extends significantly farther into the sensor cladding than that of the TE modes. For example, the simulated 1/e field penetration distance taken with respect to the electric field intensity ($|E|^2$) at the waveguide surface for the TE modes on the top surface of the waveguide is on the order of 60 nm while that of the TM modes is on the order of 110 nm, and the overall field intensity outside of the waveguide core is much higher in the TM case. The higher field of the TM modes outside the waveguide is expected to drastically increase the bulk refractive index sensitivity of these modes, as more of the modal field travels in the analyte (biological sample). Because the target molecular species used for our biosensing experiments are on the order of 5-15 nm in diameter [25, 26], they are captured during a binding assay near the sensor's surface, resulting in the measured relative peak shifts of the TE and TM modes differing from the relative bulk sensitivities. While we predict that the TM modes will be significantly more sensitive than the TE modes, the difference will not be as dramatic as it would be for bulk refractive index sensing or for very large analytes. When the particles are distant from the waveguide surface, however, we predict (from simulation) the sensitivity of the two modes to be very different; for example, at a distance of 180 nm away from the top of the 10 μm disk, the TM mode is 19 times more sensitive than the TE mode to index variations.

In order to simulate the disks' quality factors and coupling coefficients for comparison with experimental data, we employed the method previously demonstrated by our group [23]. Briefly, the FDTD method was used to simulate the point coupling between the 400 nm bus waveguide and the disk. To represent the disk in these FDTD simulations, a wide bent waveguide was used. The width of this waveguide was large enough to contain the modes we wished to analyze (5 μm wide for the 10 μm radius disk; 1.5 μm wide for the 3 μm radius disk). The mode profile from MODE Solutions was added as a source to one end of the bent waveguide and the transmitted power was monitored at the other end of the bent waveguide after the coupler. Similarly, the coupled power was monitored at the end of the bus waveguide after the point coupler region. The simulated coupling, combined with the material losses, including water absorption, obtained from MODE Solutions and an approximation of the scattering loss (taken as 10 dB/cm for the 3 μm disk and 1 dB/cm for the 10 μm disk from our experimental results) was used to determine the appropriate coupling gap as well as the predicted resonator quality factors.

#184113 - $15.00 USD Received 24 Jan 2013; revised 7 Mar 2013; accepted 9 Mar 2013; published 26 Mar 2013

The bending losses of the less-confined TM modes are higher than their TE counterparts. For example, in a disk of 5 μm radius the fundamental TE mode has a simulated bending loss of nearly zero, while the fundamental TM mode has a simulated bending loss of 4 dB/cm; as the radius is decreased the difference becomes even more apparent, with the TE and TM bending losses in a 3 μm disk being again nearly zero and 410 dB/cm, respectively. Consequently it was found that relatively large disk resonators are needed in order to support TM modes with high quality factors. Based on the losses and mode profiles determined from our simulations, disk radii of 3 μm (for the disk supporting only TE modes) and 10 μm (for the disk supporting both TE and TM modes) were chosen, both with a coupling gap of 200 nm.

To evaluate the multiplexing potential of our disk resonators [27], we cascaded two disks on the same I/O waveguide. For the multiplexing tests, one disk was exposed to the fluid in the microfluidic channel while the reference disk was kept under the polydimethylsiloxane (PDMS) polymer microchannel wall. The PDMS block with micro-molded channel (indented into the block) was aligned such that the channel indentation through which fluid could be supplied was positioned on top of one disk while the other disk was beneath the PDMS surface reversibly bonded to the nanophotonic chip. The disk in the channel served as the sensing disk while the disk under the PDMS was not influenced by any binding events.

In order to cascade the disks on the same waveguide, the disk radii were slightly varied (for the 3 μm disks, one disk had a radius of 3 μm while that of the other was 3.01 μm) to ensure that the resonance peaks from each device were located in different regions of the spectrum. The small increase in disk radius slightly increases the optical path length for a round trip in the resonator and thus increases the resonance wavelength. Using a method like that used in our disk simulations, Eq. (1) may be used to determine the resonance positions for the disks of various radius permutations and thus determine the peak spacing. Larger perturbations to the disk radius will result in larger peak spacing. For our radius permutation, we simulate a peak spacing of approximately 5 nm, based on the assumption that both disks are surrounded by the same cladding index. Fabrication tolerances as well as the difference in the cladding indices will both modify the peak spacing, as the 3 μm disk was under water while the 3.01 μm disk was surrounded by some combination of PDMS and air, depending on how the PDMS surface reversibly bonded and conformed to the disk.

3. Methods and materials

Resonant disk biosensors (Fig. 2(b)) were realized on 220 nm SOI material from Soitech (Peabody, MA) and fabricated in the University of Washington's Microfabrication Facility (MFF) using a JEOL JBX-6300FS Direct Write E-Beam Lithography System (EBL) (Peabody, MA). The EBL provides a low-cost, fast turn-around, foundry-compatible fabrication alternative that has been optimized [28–30] to produce consistent, robust, low-loss silicon photonic components [31], making the transition to a costly foundry service with high confidence.

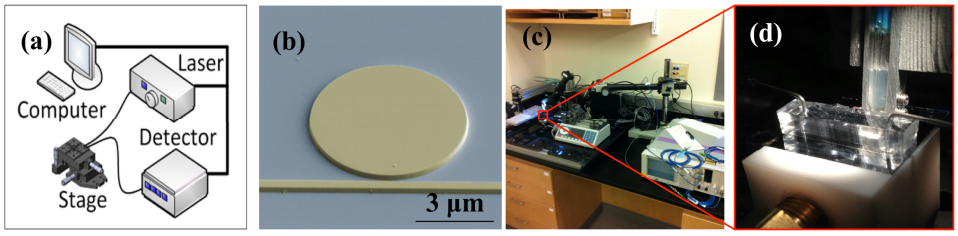

Fig. 2. (a) Schematic of our optical testing setup. (b) SEM image of a 3 μm (TE only) micro-disk resonator sensor. (c) Custom silicon photonics biosensing measurement setup. (d) PDMS flow cell with four port optical fiber connected to a 1550 nm tunable laser source.

#184113 - $15.00 USD Received 24 Jan 2013; revised 7 Mar 2013; accepted 9 Mar 2013; published 26 Mar 2013

Our test setup, shown in Fig. 2(c), is optimized for custom silicon photonic biosensing applications. A PC controls the laser, detector, and reagent sequencing to orchestrate the acquisition process (Fig. 2(a)). Microfluidic PDMS flow cells are fabricated by replica molding patterns from a mold master fabricated with standard photolithography techniques using SU-8 (MicroChem, USA) on silicon. Our optofluidic platform for device interrogation, shown in Fig. 2(d), consists of the silicon photonic sensors reversibly bonded to PDMS microfluidic chips connected to syringe pumps for solution handling.

Devices are characterized using an optical test setup that consists of a tunable laser source (Agilent 81682A, with an output wavelength range from 1460 to 1580 nm); optical power sensors (Agilent 81635A); temperature controller (SRS LDC501); microscope; and computer for data acquisition. Light is coupled on and off chip using a four-port polarization maintaining optical fiber array (PLC Connections, Columbus, OH) with two fibers aligned for TE-mode operation, and two for TM-mode operation. The fibers interface to on-chip grating couplers [32] designed to couple light into either TE or TM waveguide modes.

In order to determine the sensors' bulk refractive index sensitivities, standard solutions of 62.5 mM, 125 mM, 250 mM, 500 mM, 1M, and 2M sodium chloride were characterized with a Reichert AR200 Digital Refractometer (Depew, NY) and flowed over the sensors through our custom PDMS microfluidic channels.

To demonstrate the sensors' ability to interrogate biomolecular interactions, we performed a modified sandwich assay [33, 34] involving well characterized molecules, namely protein A (Thermo Fisher Scientific; Rockford, IL), anti-streptavidin (antiSA, Vector Labs; Burlingame, CA), streptavidin (SA, Vector Labs; Burlingame, CA), bovine serum albumin (BSA, Sigma Aldrich; St Louis, MO), and biotin-BSA (bBSA) which was conjugated per the manufacturer's instructions using a kit (SoluLink; San Diego, CA). Reagents were introduced to the sensor arrays using a reversibly bonded PDMS flow cell and Chemyx Nexus 3000 Syringe Pump (Houston, TX) at 10 μL/min. The pump was paused briefly to permit manual switching between solutions. The optofluidic stage was thermally tuned to 30°C (~5°C above ambient) to minimize thermal drift. Each sensor was equilibrated using phosphate-buffered saline (PBS) buffer for at least 20 minutes prior to beginning data acquisition and running the binding assay. The wavelength and power values of the tracked peaks were acquired every 45 seconds.

4. Results

4.1 Sensor characterization

Using aqueous NaCl solutions as refractive index standards, we determined the disks' quality factors (Q), their sensitivities, free spectral ranges (FSR), and intrinsic limits of detection (ILOD) in order to characterize their sensing performance in advance of biological experiments. We then compared these values with those predicted by the simulations outlined in section 2. This section presents the simulated and experimental sensing characteristics, and they are summarized in Table 1.

As predicted, the optical spectrum from the 3 μm disk indicated that there were two optical modes present: the fundamental (TE0) and first-order (TE1) TE modes. The FSRs from these modes are both relatively wide; as such, our spectral acquisition range only covered two resonance peaks from the TE1 mode and one peak from the TE0 mode. We observe an FSR of 38.8 nm for the TE1 mode; this is in agreement with the simulated value of 37.9 nm, well within fabrication tolerances. The quality factors of these resonance peaks were measured at approximately 33 000 (38 000 in simulation) for the TE0 peak and 22 000 (31 000 in simulation) for the TE1 peak.

We observed that the 10 μm disks are highly multimode, and their spectra contain visible resonance peaks from at least three TM modes and three TE modes. Although polarization-controlled TM light was input to and output from the chip, TE modes appear to be partially

#184113 - $15.00 USD Received 24 Jan 2013; revised 7 Mar 2013; accepted 9 Mar 2013; published 26 Mar 2013

excited in the disk alongside the TM modes. Because we measured the through port spectrum, we were able to observe both TE and TM resonance peaks. We tracked a TM resonance peak as well as a TE resonance peak in the 10 μm disk in order to compare their sensing capabilities in the same disk. In order to differentiate between the various TE and TM modes in the spectrum, we tracked the evolution of the modes in the presence of varied salt concentration, together with a measurement of the quality factors and FSRs. A comparison with simulations enables a determination of which mode is which. The peak from the TM mode exhibited an FSR of 9.66 nm (simulated 9.7 nm) and a Q of 16 000 (fundamental (TM0) mode simulated 12 000); as such, we expect that the tracked peak corresponded to the fundamental TM optical mode. The peak from the TE mode showed an FSR of 11.2 nm (simulated 10.2 nm) and a Q of 131 000 (second (TE1) mode simulated 140 000).

Figure 3 presents the calibration results for the TE and TM modes in the 3 μm and 10 μm disks identified above. Figure 3(a) depicts the raw spectrum in the spectral region around the TE0 peak of the 3 μm disk and shows the peak shift under different refractive index standards (NaCl solutions). Similarly, Fig. 3(b) depicts the shift of the TM0 peak in the 10 μm disk. Figure 3(c) shows the peak wavelength shift vs. refractive index change and fit to refractive index sensitivity for the fundamental (black) and second (green) TE modes in the 3 μm disk resonator; using this linear fit, we find refractive index sensitivities of 26 nm/RIU (simulated 28 nm/RIU) for the TE0 mode and 29 nm/RIU (simulated 32 nm/RIU) for the TE1 mode. Likewise, Fig. 3(d) depicts the peak wavelength shift vs. refractive index change and fit to refractive index sensitivity for the TM0 mode (blue) and TE1 mode (black) in the 10 μm disk resonator. We find refractive index sensitivities of 142 nm/RIU (simulated 137 nm/RIU) for the TM0 peak and 21 nm/RIU (simulated 19 nm/RIU) for a TE1 peak in the 10 μm disk.

From these results, we can calculate ILODs on the order of $1.8\text{x}10^{-3}$ for the TE0 mode in the 3 μm disk, $5.5\text{x}10^{-4}$ for the TE1 mode in the 10 μm disk and $6.8\text{x}10^{-4}$ for the TM0 mode in the same disk; these ILODs were obtained from Eq. (1). Our group has previously reviewed silicon photonic resonator sensors and compared them via the ILOD metric [2], and the very best ring resonator sensors demonstrated ILODs of $2.89\text{x}10^{-4}$ (TM) and $5.14\text{x}10^{-4}$ (TE), while those based on slot waveguides demonstrated lower ILODs of $4.06\text{x}10^{-3}$, owing to higher scattering and bending losses. Given these values, the ILODs from our disk resonators are competitive and demonstrate that disk resonators present a viable option for silicon photonic biosensing.

Table 1. Summary of simulated and experimental disk characteristics

	Simulated			Experimental			
Disk/Mode	*FSR (nm)*	*Q (x1000)*	*S (nm/RIU)*	*FSR (nm)*	*Q (x1000)*	*S (nm/RIU)*	*ILOD (RIU)*
3 μm TE0	37.9	38	28	*N/A**	33	26	$1.8\text{x}10^{-3}$
3 μm TE1	37.9	31	32	38.8	22	29	$2.4\text{x}10^{-3}$
10 μm TM0	9.7	12	137	9.66	16	142	$6.8\text{x}10^{-4}$
10 μm TE1	10.2	140	19	11.2	131	21	$5.5\text{x}10^{-4}$

*Not measured.

#184113 - $15.00 USD Received 24 Jan 2013; revised 7 Mar 2013; accepted 9 Mar 2013; published 26 Mar 2013

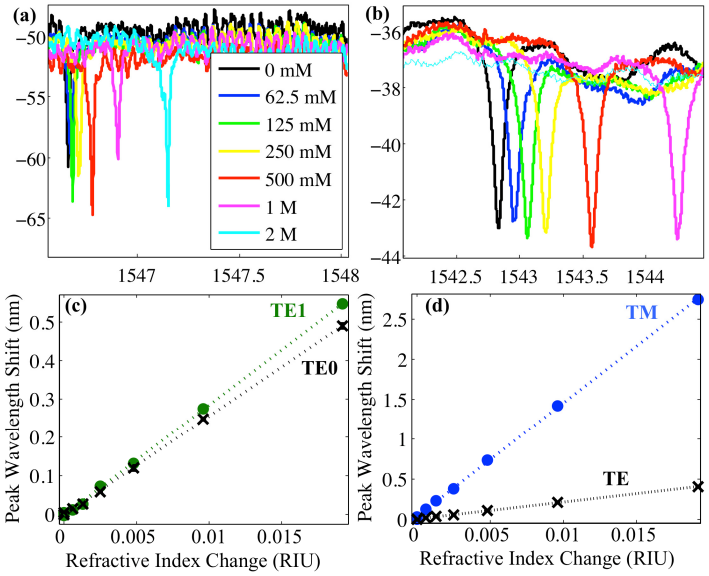

Fig. 3. Raw spectra from a TE mode in the 3 µm disk sensor (a) and a TM mode in the 10 µm sensor under varying salt concentrations (b). Peak wavelength shift vs. refractive index change and fit to refractive index sensitivity for the fundamental (black, 'X') and second (green, dot) TE modes in the 3 µm disk resonator (c) and a TM mode (blue, dot) and TE mode (black, 'X') in the 10 µm disk resonator (d). We find refractive index sensitivities of 26 nm/RIU for the fundamental TE mode and 29 nm/RIU for the second TE mode in the 3 µm disk, and 142 nm/RIU for a TM and 21 nm/RIU for a TE mode in the 10 µm disk.

Figure 4 shows an SEM image of two multiplexed disk resonators as well as the raw spectra from the two multiplexed 3 µm disks presented in this paper (one sensing disk and one disk under the PDMS) during the refractive index calibration experiment. As a result of our multiplexing experiments, we found that the clean, wide-FSR, two-mode spectra of the 3 µm disks lent themselves very well to multiplexing. The sensing peak was observed to clearly shift under the refractive index standards while the peak from the resonator under the PDMS channel wall was stationary. The peaks for both modes from the two resonators are clearly observable in the spectrum. Given the same 10 nm radius permutation used in this work, four resonators could be measurable within the FSR (and within the spacing between the peaks from the two modes) without their peaks interfering; as such, the 3 µm disks show great promise for their potential to be multiplexed. However, the highly multimode nature of the 10 µm disk resonators complicates their use in multiplexing as many resonance peaks were observed in their spectra.

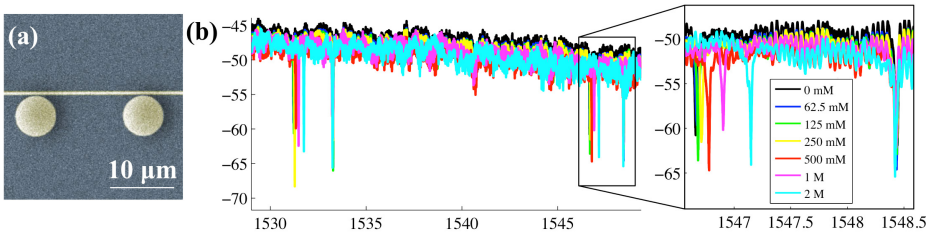

Fig. 4. (a) SEM image of two resonators multiplexed on the same I/O pair. (b) Optical spectrum under varying NaCl solutions from two 3 µm disk resonators multiplexed on the same I/O pair, with zoom inset showing the sensing peak shift along with the stationary peak from the resonator under PDMS for the fundamental mode.

#184113 - $15.00 USD Received 24 Jan 2013; revised 7 Mar 2013; accepted 9 Mar 2013; published 26 Mar 2013

4.2 Biosensing demonstration

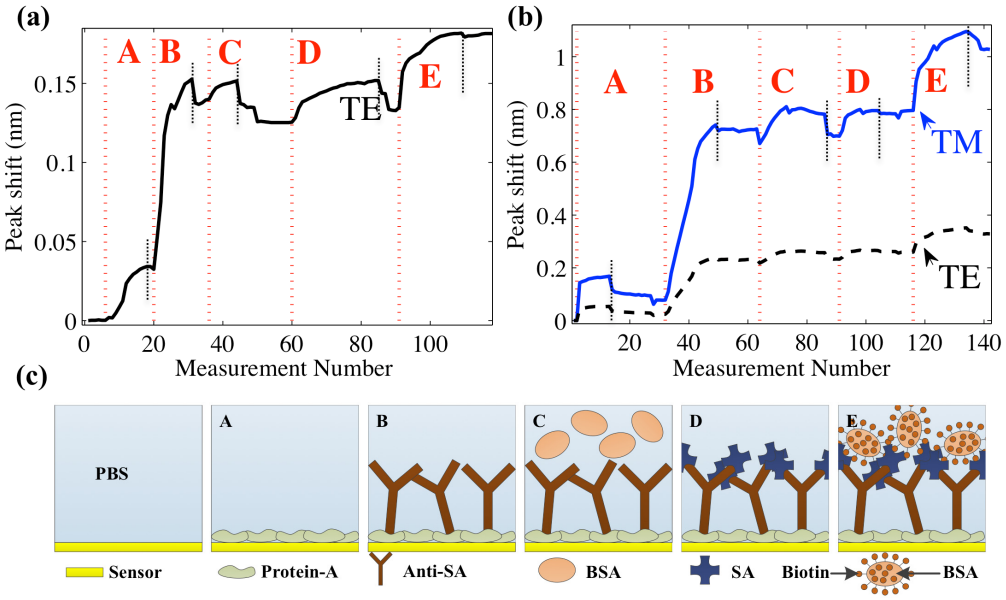

Fig. 5. Biosensing results for the 3 μm (a) and 10 μm (b) disk sensors. (b) Resonance peak shifts (in nm) of the TM (blue) and TE (black, dashed) modes in the 10 μm disk. (a) Resonance peak shift (in nm) of the fundamental TE-like mode in the 3 μm disk. (c) Reagent sequencing corresponding to regions [A-E] in (a) and (b). Region A = protein A (1 mg/mL), B = anti-streptavidin (SA) (125 ug/mL), C = Bovine Serum Albumen (BSA) (2 mg/mL), D = streptavidin (SA) (108 μg/mL), E = Biotin-BSA (2.5 mg/mL). Introduction of reagent in each region was followed by a PBS wash, indicated by the short dashed black line within each region.

As shown in Figs. 5(a) and 5(b), we demonstrate the biosensing capability of the 3 μm TE and 10 μm TE/TM disks respectively. For the purpose of assessing the biological performance of our disk resonator devices, we developed a modified sandwich assay to interrogate multiple modes of specific and non-specific biomolecular interactions, as illustrated in Fig. 5(c). The introduction of each reagent was followed by a PBS buffer rinse (10 min), as indicated by the black-dashed line within each region. First, protein A (1 mg/mL) was passively adsorbed to the native oxide of the sensor's surface. Originally derived from the bacterium *Staphylococcus aureus*, protein A is a protein that has a high affinity for human and mouse antibodies (IgG), and is able to facilitate the orientation of capture antibodies to a solid substrate [35, 36]. Physisorption, or irreversible binding of proteins to a surface (region [A] in Fig. 5), such as protein adsorption to the surface oxide is a well-known phenomenon in biomaterials science, and can be used to enable rapid surface functionalization with protein [37, 38]. While covalent methods for surface modification support more robust surface chemistries for lengthy biological assays, physisorption is sufficient for preliminary validation purposes. As illustrated in region [B] of Fig. 5, the antibody antiSA (125 μg/mL) was captured and oriented on the sensor's surface by the immobilized protein A layer. Sudden changes (drops) in the observed refractive index, as illustrated in regions [B, C, and D] of Fig. 5(a), are due to the introduction of bubbles while switching biological solutions. Slight decreases following buffer changes can also be due to partial desorption of the physisorbed protein A anchoring layer used to capture the IgG (antiSA). It has previously been shown that physisorbed protein A forms multiple add layers that facilitate IgG capture [39]. These multi-layer physisorbates are susceptible to limited desorption of functional protein A-antibody conjugates, particularly during buffer change or inadvertent introduction of air bubbles during

#184113 - $15.00 USD Received 24 Jan 2013; revised 7 Mar 2013; accepted 9 Mar 2013; published 26 Mar 2013

sample handling, but they will not produce sudden drops in sensor response. While both bubbles and protein A desorption can introduce slight resonance shifts, they do not alter subsequent biological interactions beyond small reductions in the number of available binding receptors on the sensor surface. After rinsing with buffer to remove unbound antibody, the sensor was challenged with non-specific protein BSA (2 mg/mL) as a negative control to demonstrate the ability of the antibody-functionalized disk sensors to resist off-target binding (region [C]). Due to minimal non-specific BSA adsorption to the sensor's surface, the sensor wavelength shift approaches the pre-BSA baseline after exposure to BSA. While the non-specific interactions were minimal in this particular study, non-specific protein adsorption is a common challenge for label-free optical biosensors; we have previously demonstrated the ability to eliminate non-specific protein adsorption in undiluted human plasma using novel zwitterionic surface chemistries [17].

To validate the functional sensor's ability to capture specific biological species, we introduced SA (108 μg/mL) which was bound by the immobilized anti-SA antibody, resulting in a significant and irreversible shift in the resonance wavelength of the sensor as shown in region [D]. The captured SA retained its biological function, as determined by binding of biotinylated-BSA to the SA as shown in region [E]. While it is unlikely that all four SA binding sites are occupied with BSA-biotin, the observed wavelength shift results are consistent with an average of a 2.5:1 ratio of biotin-BSA:SA. Since the surface has been previously passivated by BSA, we are confident that this binding interaction is specific, and is not necessarily precluded by sterics. Given the virtually irreversible biotin-BSA interaction, our past experience with biotin-BSA binding assays support our observation of 60-70% saturation following 10-15 minutes of binding. In addition to validating retained bioactivity of the surface captured species, the multi-step sandwich assay illustrates the suitability of the disk biosensors with multi-layer biological assays.

It is worth noting that the relative resonance wavelength shifts for each captured biomolecule corresponded well to the expected refractive index shift based on their respective molecular weights [25, 26]. We also validated the resonance wavelength shift for the first step of our bioassay on the 10 μm disk (region A in Fig. 5(c)) using thin protein layer simulations in the Lumerical MODE Solutions eigenmode solver. Protein A, a 42 kDa globular protein, has a diameter of approximately 3 nm [40, 41] and refractive index of 1.48 [42]. Coen et al has previously observed that the first protein A adlayer denatured and resulted in a 1 nm thick, biologically inactive film [39]. They also observed that a second layer of protein A formed on top of the first, providing active receptor to bind the Fc domain of IgG. Therefore, we assume that our sensor has a physisorbed layer of protein A ($n = 1.48$) between 1 and 3 nm thick cladded by PBS buffer ($n = 1.35$); these parameters were used for our thin layer simulations in the eigenmode solver. Similar to how the bulk refractive index simulations were conducted, as discussed in section 2, the eigenmode solver was used to determine the modal effective index for the sensor with and without a 1 nm or 3 nm protein A layer; these effective indices were then plotted with the resonance equation (Eq. (1) to determine the resonance wavelength shift induced by the addition of the protein layer and these shifts were compared with the observed experimental shifts.

For the TM0 mode, our simulations indicate that a 1 nm layer would need to cover 41.4% of the sensor's surface to result in the observed experimental wavelength shift of 98.5 pm. Likewise, a 3 nm layer would need to cover 13.7% of the surface to result in a similar wavelength shift. For TE1, a 1 nm layer would need to cover 51.9% of the sensor's surface to result in the observed experimental wavelength shift of 30 pm. Likewise, a 3 nm layer would need to cover 17.1% of the surface to result in a similar wavelength shift. The slightly larger apparent coverage for TE results from the different sensing region of this mode (being a first-order mode, the sensing region for TE1 extends further inwards into the disk than that of the fundamental TM0 mode) and is not significant. Our results are within the range of surface coverage also observed by Coen et al.

#184113 - $15.00 USD Received 24 Jan 2013; revised 7 Mar 2013; accepted 9 Mar 2013; published 26 Mar 2013

As subsequent layers of captured protein are unlikely to achieve a complete monolayer, the total film thickness of the captured biological multi-layer is estimated to be between 15 and 30 nm. This estimate is based on the approximate sizes of the immobilized species. This region of biomolecule capture is well within all of the tracked modes' calculated evanescent fields. Although the bulk refractive index sensitivity of the TM0 mode was found to be approximately six times that of the TE1 mode, the peak shift corresponding to the TM0 mode is approximately three times that of the TE1 mode. As discussed in the simulation section, this apparent discrepancy may be understood by comparing the mode profiles of the different modes (shown in Fig. 1). The TM mode profile extends much further away from the surface of the waveguide than the TE profile, rendering it much more sensitive to bulk changes. However, during the "sandwich" assay, molecules bind closely to the surface of the waveguide and, as expected, the differential sensitivity (measured shift of the TM mode compared to that of the TE mode) is not as dramatic as it is in the bulk case.

5. Conclusion

We have demonstrated competitive sensing performance using compact micro-disk resonators optimized for multiplexed biosensing applications, and verified our design process by comparing their performance with numerical simulations. The ILODs from our disk resonators are competitive with the best ring-based sensors, while the disk geometry offers potential advantages such as a small footprint and wide FSR, which are advantageous for multiplexing applications. Furthermore, there is potential to improve the disks' sensing performance by optimizing the coupling condition of the resonators and by moving to lower wavelengths of light where the water absorption is weaker; both of these methods would increase the resonator Q and thus improve the ILOD. The 3 μm disks showed a sensitivity of 26 nm/RIU and quality factor of 33 000, yielding an ILOD of $1.8\text{x}10^{-3}$ for the fundamental TE mode, and both observed modes yielded wide FSRs on the order of 35-40 nm. Because the TE electric field density is concentrated close to the disk surface, these TE disks are ideally suited for sensing biomolecules (1-20 nm particles) that bind closely to the surface of the disk. The disks' small footprints and wide FSRs also facilitates multiplexed applications, including cascaded micro-disk sensors.

Our 10 μm multi-modal disks exhibited a sensitivity of 142 nm/RIU and quality factor of 16 000 for the tracked TM mode, yielding an ILOD of $6.8\text{x}10^{-4}$ and FSR of 9.66 nm. The TE mode in this same disk had a sensitivity of 21 nm/RIU and quality factor of 131 000, resulting in an ILOD of $5.5\text{x}10^{-4}$. We hypothesize that the extended evanescent field profile of the TM mode will permit sensing of biomolecules that bind to the sensor via long stand-off functionalization chemistries. This characteristic will permit the use of polymer coatings that may keep the analyte's mass a significant distance from the sensor's surface. The deeper penetration of the TM mode evanescent field should also support detection of large particles, including viruses (20 - 200 nm), bacteria (500 – 1000 nm), and cells (5 – 20 μm). In addition, it may be possible to harness the unique multimode property of the 10 μm disk resonators for biosensing applications [43]. The different mode profiles of the TE and TM modes could provide additional sensing information in addition to that provided by single mode sensing systems. For instance, it may be possible to gauge refractive index changes and also size measurements of biospecies from two peaks in a single sensor. This could permit sensing that can distinguish whole cells from proteins binding to the sensor surface.

Based on the results for the cascaded disks, we have demonstrated that multiple sensors can be multiplexed on the same waveguide bus, leveraging the large FSR of small micro-disk resonators. The number of disks that can be interrogated by the same I/O waveguide for a given experiment is limited by the peak spacing between the mode of interest and the next closest resonance peak (from the same mode or from another mode in the same disk), as well as the overall peak shift expected in the experiment of interest and the fabrication resolution. Fabrication nonuniformities in the widths and thicknesses of the structures may also play a

#184113 - $15.00 USD Received 24 Jan 2013; revised 7 Mar 2013; accepted 9 Mar 2013; published 26 Mar 2013

role (it is difficult to control exactly where in the spectrum the resonance peaks will lie for a given resonator). However, because the disks are quite small and close together, the fabrication errors for the multiplexed disks should be highly correlated. Our 3 μm disks using the current 10 nm radius perturbation should permit up to four multiplexed sensors; reducing the radius perturbation to 5 nm would permit eight disks. This type of multiplexing will not only support the inclusion of built-in thermal references and control disks, but it will also allow simultaneous detection of multiple biological species—an important feature for a medical diagnostic. With device refinement, it will be possible to reduce the number of modes present in the 10 μm disk (and thus simplify their complex spectra) and perhaps the 3 μm disk (nearly doubling the multiplexing limit by removing the TE1 mode) by moving from a 'disk' towards a 'doughnut' shaped footprint while still minimizing the interaction of the fundamental mode with the doughnut's inner sidewall. Finally, it is possible to leverage the surface functionalization strategies and chemistries recently published by our group [17] to demonstrate clinically relevant assays in complex samples using our custom, matrixed biosensors—moving this technology one step closer to a viable medical diagnostic device.

Acknowledgments

This work was supported by the University of Washington (UW) Royalty Research Fund, NSF CBET (Award no. 0930411), and the Washington Research Foundation. We gratefully acknowledge Lumerical Solutions, Inc. for providing the simulation software, and the Centre for High-Throughput Phenogenomics at the University of British Columbia (UBC) for assistance with SEM imaging. We are also grateful to Mitchell Webb and Matt Doerfler for their efforts in preliminary simulations and data analysis preceding this work. Part of this work was conducted at the University of Washington Microfabrication/Nanotechnology User Facility, a member of the NSF National Nanotechnology Infrastructure Network. The authors also wish to thank Professors Michael Hochberg and Tom Baehr-Jones, Dr. Ali Ayazi, and Michael Gould for insightful discussions, lab support, and the use of their optical test setup.

#184113 - $15.00 USD Received 24 Jan 2013; revised 7 Mar 2013; accepted 9 Mar 2013; published 26 Mar 2013